Received: 27 March 2023 | Revised: 29 May 2023 | Accepted: 14 June 2023

DOI: 10.4218/etrij.2023-0048

ORIGINAL ARTICLE

ETRI Journal WILEY

Nonorthogonal multiple access multiple input multiple output communications with harvested energy: Performance evaluation

Toi Le-Thanh [1,2,3] | **Khuong Ho-Van** [1,2]

[1]Faculty of Electrical and Electronics Engineering, Ho Chi Minh City University of Technology, Ho Chi Minh City, Vietnam

[2]Vietnam National University Ho Chi Minh City, Ho Chi Minh City, Vietnam

[3]Faculty of Electrical and Electronics Technology, Ho Chi Minh City University of Food Industry, Ho Chi Minh City, Vietnam

Correspondence
Khuong Ho-Van, Faculty of Electrical and Electronics Engineering, Ho Chi Minh City University of Technology, Ho Chi Minh City, Vietnam.
Email: hvkhuong@hcmut.edu.vn

Funding information
Vietnam National University Ho Chi Minh City (VNU-HCM), Grant/Award Number: B2023-20-08

Abstract

This paper demonstrates improved throughput and energy efficiency of wireless communications by exploiting nonorthogonal multiple access (NOMA), multiple input–multiple output (MIMO), and radio frequency energy harvesting (EH) technologies. To assess the performance of NOMA MIMO communications with EH (MMe), we consider the nonlinear characteristics of EH devices and propose explicit expressions for throughput and outage probability. Based on our results, the system performance is significantly mitigated by EH nonlinearity and is considerably improved by increasing the number of antennas. Additionally, by appropriately adjusting the system parameters, our NOMA MMe innovation can avert complete outages while optimizing system performance. Moreover, the results demonstrate the superiority of the NOMA MMe over its orthogonal multiple access MMe counterparts.

KEYWORDS

multiple input–multiple output, nonlinear energy harvesting, nonorthogonal multiple access, performance evaluation, Rayleigh fading

1 | INTRODUCTION

1.1 | Fundamentals

Modern 5G/6G wireless networks must provide diversified communication services for a large number of users while ensuring service quality [1, 2]. Nevertheless, current spectrum shortages and energy-saving policies pose critical challenges to the design of such networks. Therefore, additional throughput and energy efficiency countermeasures are needed.

A promising method is nonorthogonal multiple access (NOMA) [3, 4] as it attains high throughput due to the overlapping transmissions of different users based on their distinct transmit power levels within the same frequency band. Notably, sequential decoding in combination with interference cancelation can be carried out to ensure low outage probabilities (OPs). To improve energy efficiency, NOMA users can harvest radio frequency energy inherently available in the environment, such as from high-power television and radio broadcast facilities. Notably, 5G/6G users are already equipped with affordable energy harvesting (EH) circuits [5, 6]. Interestingly, the literature has focused only on the linear EH (lEH) characteristics needed to analyze basic system performance [7–12]. However, EH circuits comprise non-linear components, such as capacitors, diodes, and inductors. Thus, to more precisely and realistically measure system performance, non-lEH (nlEH) characteristics must be modeled. Thus far, several nlEH models have been proposed, including [13–19].

Our NOMA multiple input–multiple output (MIMO) communications with harvested energy (nOMMe) is shown in Figure 1. It enables a source (S) to broadcast a NOMA signal to far (D1) and near (D2) destinations. To self-power its transmissions, S must harvest energy from a power beacon (B). In addition to the throughput improvements provided by NOMA, nOMMe benefits from high throughput and energy efficiency via multiple antenna deployments for all users. Notably, the multiple antennas at Sites B and S help S harvest energy more efficiently and stably, which improves overall EH efficiency. Furthermore, multiple antennas offer more throughput options based on the antenna array processing (AAP) at the D2 site. Specifically, with multiple antennas, Site S can simultaneously transmit multiple data streams on multiple antennas to D1 and D2 to increase the data rate. Furthermore, D1 and D2 destinations can implement AAP methods, such as zero-forcing (ZF) detection, to reduce the OP [20]. As such, NOMA communications with the harvested energy for all multi-antenna users in Figure 1 is expected to achieve high energy efficiency and system throughput (TP). Nevertheless, the TP and OP of the nOMMe under nlEH have not been analyzed to verify whether it provides these advantages. Hence, this study is the first to do so.

1.2 | Existing works

The authors of [17] investigated uplink NOMA communications with EH (nOe), where various NOMA sources transmitting information to the same destination require two phases to complete the EH and information transmission (IT), as illustrated in Figure 1. Site B supplies energy to NOMA sources through wireless power

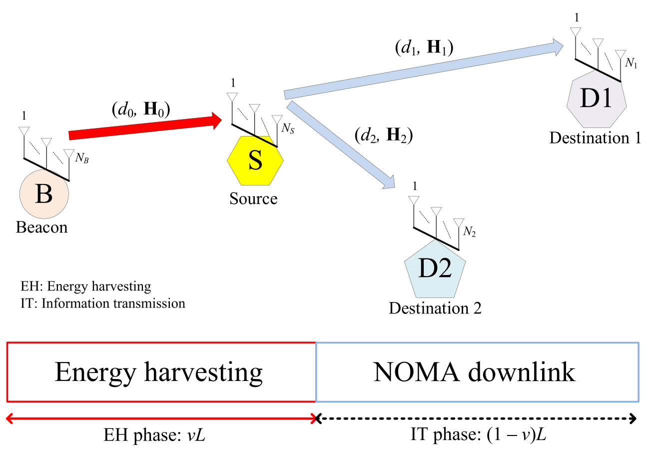

FIGURE 1 Proposed NOMA MIMO communications with harvested energy.

transfers during EH. During the IT phase, all NOMA users broadcast their information to the same destination. The authors of [17] optimized the EH duration by considering nlEH, but their average secrecy OP formula was not explicitly explained. The authors of [21] studied the special scenario of [17] using two NOMA sources. Subsequently, [21] proposed a user grouping scheme to maximize the energy efficiency of nlEH, providing a good OP approximate analysis.

Downlink nOe was investigated in [22–24], where S site broadcasts NOMA signals to D1 and D2 destinations. Then, [25] extended the works of [22–24] to include many destinations. The researchers of [22–25] provided approximate analyses of the OP and TP, and [25] maximized the sum rates. Although site S harvests wireless energy using single [22, 23] or multiple antennas [25], its processes are based on lEH, which is unrealistic in real-world applications. Moreover, D2 site scavenges wireless energy from S site using single antennas with nlEH [24]; nevertheless, the scavenged energy is unclear for what purpose. By exploiting feedback messages, [24] recommended three communication mechanisms.

A downlink nOe with D1 and D2 destinations was later studied, in which a transmission to D1 was aided by a relay designed by [26–28]. The D2 case was also considered [29–33], which scavenges energy from a NOMA source. The authors of [28] and [29] considered a nlEH method at a relay and presented an approximate analysis of the OP. Meanwhile, [26] maximized the sum rate for the lEH case, and [31] and [32] optimized a D2 site's data speed and both the entire transmission power and energy efficiency for the nlEH case, respectively. Extending the study in [28] to the context of multiple relays, [34] and [35] proposed a relay selection to aid NOMA communications from Site S to D1 and D2 destinations. Furthermore, [36] extended the work of [28] to include two relays that exchange roles to support D1. The authors of [36] later presented a throughput analysis, but it lacked the specificity needed for major improvements. In contrast, to utilize multiple relays [34, 35], [37] considered the case of multiple D2 destinations in which only one is selected to support the D1 destination. The authors of [38] and [39] extended the work of [28] to include multiple destinations. However, [27, 30, 33–39] analyzed the system performance for the lEH case. As an alternative relaying method, an intelligent reflecting surface was used as a relay to forward data from Site S to D1 and D2 [40–42]. The sum rate of the nlEH was optimized in [40] and that of lEH was optimized in [41, 42]. However, no performance analysis was mentioned in [26, 31, 32, 40–42].

In summary, [17, 21–38, 41, 42] studied trivial system models with single-antenna NOMA users to exploit APP methods for performance enhancements. However, only [39] considered all multiple antenna users.

TABLE 1 Literature review.

Reference	All multiantenna users?	nlEH consideration?	Performance analysis in closed-form?	Downlink NOMA communications?
[17]	No	Yes	No	No
[21]	No	Yes	Yes	No
[22]	No	No	Yes	Yes
[23]	No	No	Yes	Yes
[24]	No	Yes	Yes	Yes
[25]	No	No	Yes	Yes
[26]	No	No	No	Yes
[27]	No	No	Yes	Yes
[28]	No	Yes	Yes	Yes
[29]	No	Yes	Yes	Yes
[30]	No	No	Yes	Yes
[31]	No	Yes	No	Yes
[32]	No	Yes	No	Yes
[33]	No	No	Yes	Yes
[34]	No	No	Yes	Yes
[35]	No	No	Yes	Yes
[36]	No	No	No	Yes
[37]	No	No	Yes	Yes
[38]	No	No	Yes	Yes
[39]	Yes	No	Yes	Yes
[40]	No	Yes	No	Yes
[41]	No	No	No	Yes
[42]	No	No	No	Yes
Our work	Yes	Yes	Yes	Yes

Consequently, the literature does not present OP and TP analyses for the system model shown in Figure 1, which leverages nlEH and all multiantenna users so that more energy may be harvested at Site S. Theoretically, data can be transmitted at a higher rate at Site S by exploiting the multiplexing gain of the antenna array, and a better throughput can be achieved at D1 and D2 destinations by applying APP methods. In this study, we analyze the OP and TP of this system model for the first time, which provides rapid rating and optimization of TP and OP for realistic implementations. Table 1 summarizes the differences between our study and the related ones.

1.3 | Contributions

The contributions of this study are as follows:

- We propose the nOMMe in Figure 1, in which all users (B, S, D1, and D2) employ multiple antennas to improve energy efficiency and system throughput. Furthermore, we appropriately characterize nlEH circuits for our model[a] in [13] at Site S.
- For a prompt performance evaluation, we present the OP and TP analyses for the proposed nOMMe considering EH nonlinearity.
- We rate and optimize nOMMe's system performance in numerous practical contexts, showing that EH nonlinearity considerably deteriorates system performance, which is strongly mitigated by accreting the number of antennas. Moreover, the nOMMe model averts complete outages and attains optimum throughput by appropriately setting system parameters. Furthermore, the nOMMe is considerably

[a]Note that diverse nlEH models have been proposed in many works, including [13–19]. Among these, the model in [13] is widely applied to performance analysis problems as its characteristic renders the analysis tractable [28, 29, 40].

superior to OMA MIMO communications with EH (OMMe) counterparts.

1.4 | Paper structure

Section 2 describes the proposed nOMMe, and Section 3 presents its OP and TP analyses. Section 4 derives upper bounds for OP and TP corresponding to high transmit power and lEH scenarios. Section 5 discusses the theoretical and simulated results from numerous realistic contexts. Finally, Section 6 concludes this paper. The detailed derivations in Sections 3 and 4 and the OMMe's OP and TP analyses are presented in Appendices A and B, respectively.

2 | NOMME

Figure 1 depicts the basic nOMMe system model[b] comprising Sites B, S, D1, and D2. This model exemplifies downlink communications in a mobile system. Site S is assumed to be power-limited; thus, it must scavenge energy from Site B, which can be configured as a dedicated power beacon, just like a radio/television broadcasting station. In the proposed system model, Site B powers the operation of Site S during the EH phase, which has a νL duration, where $\nu \in (0,1)$ is the time-splitting factor. However, Site S creates the NOMA signal to broadcast to the D1 and D2 destinations during the IT phase whose duration is $(1-\nu)L$. To improve both EH efficiency and system throughput, Sites B, S, D1, and D2 are, respectively, equipped with N_B, N_S, N_1, and N_2 antennas. Multiple antennas enable the S site to efficiently scavenge energy from the multiantenna power beacon, B site, during the EH phase for improved efficiency. The S site then transmits multiple parallel data streams through S–Dd MIMO channels during the IT phase for improved spectral efficiency by exploiting the multiplexing gain of MIMO channels. Additional throughput improvements can be provided by applying AAP methods at the Dd site, where $d=\{1,2\}$. Furthermore, $N_d \geq N_S$ is assumed to be capable of detecting signals at Dd over the S–Dd MIMO channel.

Let $\mathbf{H}_0$, $\mathbf{H}_1$, and $\mathbf{H}_2$ denote channel matrices of sizes $N_S \times N_B$, $N_1 \times N_S$, and $N_2 \times N_S$, respectively, which represent the MIMO channels between Sites B and S, S and D1, and S and D2, respectively. Rayleigh fading is assumed for all channels; hence, entries of $\mathbf{H}_i$ and $i=\{0, 1, 2\}$, represent independent and identically distributed (iid) complex Gaussian random variables (rv's), where $[\mathbf{H}_i]_{mn} \sim \mathrm{N}(0, \varphi_i)$. To account for path-loss effects, we model $\varphi_i = \rho \lambda_i^{-\mu}$ where μ is the path-loss decay, λ_i is the corresponding transmitter-to-receiver distance, and ρ is the fading power at a reference distance of 1 m [14].

As seen in Figure 1, Site B powers Site S via a wireless power transfer through the MIMO channel, $\mathbf{H}_0$, during the EH phase. This considerably increases the quantity of scavenged energy at Site S and ultimately improves the overall throughput. As a result, site S scavenges $E_S = \nu L \tau (P/N_B) \|\mathbf{H}_0\|^2$, where $\|\mathbf{H}_0\|^2 = \sum_{u=1}^{N_S}\sum_{v=1}^{N_B} \left|[\mathbf{H}_0]_{uv}\right|^2$ is the squared Frobenius norm of $\mathbf{H}_0$. P is the entire transmit power of Site B, which implies that P/N_B is the transmit power of the B site's antenna, and $\tau \in (0,1)$ is the energy conversion efficiency. Because the IT phase has a duration of $(1-\nu)L$, the power converted from E_S is $E_S/((1-\nu)L)$, which may be used by Site S to communicate with D1 and D2 destinations during the IT phase. However, owing to nlEH characteristics [13], Site S transmits the NOMA signal during the IT phase with the following power:

$$P_S = \begin{cases} \frac{\tau\nu}{1-\nu}\frac{P}{N_B}\|\mathbf{H}_0\|^2, & \nu\frac{P}{N_B}\|\mathbf{H}_0\|^2 \leq \Omega, \\ \frac{\tau\nu\Omega}{1-\nu}, & \nu\frac{P}{N_B}\|\mathbf{H}_0\|^2 > \Omega, \end{cases} \quad (1)$$
$$= \begin{cases} U\Theta, & \Theta \leq G, \\ J, & \Theta > G, \end{cases}$$

where Ω is the power saturation threshold, $U = (\tau\nu/(1-\nu))(P/N_B)$, $J = \tau\nu\Omega/(1-\nu)$, $G = (\Omega/\nu)(N_B/P)$, and $\Theta = \|\mathbf{H}_0\|^2$.

Notably, (1) precisely reflects the nlEH characteristics. Specifically, when the input power does not exceed Ω, the output power is $U\Theta$, which is linearly proportional to the input power; otherwise, the output power will become saturated at Ω. Furthermore, when Ω is high ($\Omega \to \infty$), nlEH becomes lEH, as anticipated.

During the IT phase, Site S sends an $N_S \times 1$ signal vector, $\mathbf{x}$, with N_S symbols in the form of a NOMA signal to the D1 and D2 destinations (Table 2). This implies that the n^{th} entry of vector $\mathbf{x}$ has the form, $x_n = \sqrt{\psi}x_{1n} + \sqrt{1-\psi}x_{2n}$, where x_{1n} and x_{2n} are individual symbols intended for Sites D1 and D2, respectively. Here, $\mathsf{E}\{|x_{1n}|^2\} = \mathsf{E}\{|x_{2n}|^2\} = 1$ and ψ is the power percentage allotted for transmitting x_{1n}. According to the NOMA principle, D1 is the farther destination, whereas D2 is the closer station. x_{1n} is therefore allocated more power than

[b]Our work studies the NOMA of each cluster at two destinations, as a high number of destinations in each cluster is shown to increase complexity while reducing efficiency [43, 44]. A two-destination NOMA configuration was integrated into 3GPP-LTE-A [45, 46]. Nevertheless, grouped pairs of destinations are beyond the scope of this study. Interested researchers should read [4, 21, 31, 34, 47] for a complete explanation of this issue.

TABLE 2 Frequently used symbols.

Symbol	Interpretation
τ	Energy converting efficiency
ρ	Fading power at the reference distance
$[\mathbf{G}]_{mn}$	Entry at row m^{th} and column n^{th} of matrix $\mathbf{G}$
$[\mathbf{m}]_n$	The n^{th} entry of vector $\mathbf{m}$
$\mathbf{G}^*$	Conjugate transpose of matrix $\mathbf{G}$
$\mathsf{E}\{\cdot\}$	Expectation operator
$\gamma(\cdot,\cdot)$	Incomplete lower Gamma function
$\mathbf{y}$	Received signal vector
$\overline{F}_Y(\cdot)$	Complementary cumulative distribution function (CCDF) of Y
$\mathbf{H}$	Channel matrix
$f_Y(\cdot)$	Probability density function (PDF) of Y
$\Pr\{\cdot\}$	Probability operator
$\Gamma(\cdot)$	Complete gamma function
$\mathbf{v}$	Additive noise vector
$F_Y(\cdot)$	Cumulative distribution function (CDF) of Y
$\mathsf{N}(0,j)$	Zero-mean and j-variance complex Gaussian random variable
$\mathsf{K}_b(\cdot)$	Modified Bessel function of the second kind of order b
$\mathbf{x}$	Transmit signal vector
ν	Time-splitting factor
d_0	Distance from B to S
d_1	Distance from S to D1
d_2	Distance from S to D2
N_B	Number of antennas at B
N_S	Number of antennas at S
N_1	Number of antennas at D1
N_2	Number of antennas at D2
L	Total time of two phases
μ	Path-loss exponent
P	Entire transmit power of B
Ω	Power saturation threshold
ψ	Power percentage allotted for transmitting x_{1n}
ε	Noise variance
K	Target spectral efficiency
Δ_d	Overall OP at Dd
Δ_{dn}	OP of the n^{th} symbol stream at Dd
$\mathbb{T}_d$	Throughput of Dd

x_{2n}; hence, $\psi > 0.5$. Accordingly, Dd, $d = \{1, 2\}$, receives an $N_d \times 1$ signal vector as follows:

$$\mathbf{y}_d = \mathbf{H}_d \sqrt{\frac{P_S}{N_S}} \mathbf{x} + \mathbf{v}_d, \tag{2}$$

where $\mathbf{v}_d$ is the $N_d \times 1$ noise vector at Dd, and the n^{th} entry is $[\mathbf{v}_d]_n \sim \mathsf{N}(0, \varepsilon)$.

Dd recovers its desired information, x_{dn}, via two-step signal detection, where MIMO detection is performed in Step 1 to recover the NOMA signal, x_n, and NOMA detection is carried out in Step 2 to restore the individual signal, x_{dn}. In this study, MIMO detection is illustrated as ZF detection [20]. However, other MIMO detections, such as minimum mean squared error detection, which are relatively more complicated but attain better performance, can be employed. Based on the ZF detection, the received signal vector, $\mathbf{y}_d$, is first multiplied by $\sqrt{(N_S/P_S)}\left(\mathbf{H}_d^* \mathbf{H}_d\right)^{-1} \mathbf{H}_d^*$, resulting in

$$\begin{aligned} \tilde{y}_d &= \sqrt{\frac{N_S}{P_S}} \left(\mathbf{H}_d^* \mathbf{H}_d\right)^{-1} \mathbf{H}_d^* \mathbf{y}_d \\ &= \mathbf{x} + \sqrt{\frac{N_S}{P_S}} \left(\mathbf{H}_d^* \mathbf{H}_d\right)^{-1} \mathbf{H}_d^* \mathbf{v}_d. \end{aligned} \tag{3}$$

From (3), we can see that the ZF detection decouples the received signal vector, $\mathbf{y}_d$, into N_S symbol streams, where the n^{th} symbol stream is rewritten as

$$[\tilde{y}_d]_n = \sqrt{\psi} x_{1n} + \sqrt{1-\psi} x_{2n} + [\tilde{v}_d]_n, \tag{4}$$

where $[\tilde{v}_d]_n = \left[\sqrt{(N_S/P_S)}\left(\mathbf{H}_d^* \mathbf{H}_d\right)^{-1} \mathbf{H}_d^* \mathbf{v}_d\right]_n$.

Based on (4), Dd decodes its desired symbol, x_{dn}, as governed by NOMA detection. Because $\psi > 0.5$, Site D1 restores its private symbol, x_{1n}, directly from $[\tilde{y}_1]_n$ without recovering x_{2n}. Consequently, the signal-to-interference plus noise ratio (SINR) needed for Site D1 to recover x_{1n} from (4) is

$$\begin{aligned} \Lambda_1^{x_{1n}} &= \frac{\psi}{\Xi\left\{\left|\sqrt{1-\psi} x_{2n} + [\tilde{v}_1]_n\right|^2\right\}} \\ &= \frac{\psi}{1-\psi+\Phi_{1n}}, \end{aligned} \tag{5}$$

where $\Phi_{dn} = \Xi\left\{\left|[\tilde{v}_d]_n\right|^2\right\}$, $d = \{1, 2\}$.

Because $\psi > 0.5$, Site D2 first restores the D1 site's message, x_{1n}, using x_{2n} for the interference and subsequently removes it[c] induced by x_{1n} before recovering its private symbol, x_{2n}. Accordingly, Site D2 recovers x_{1n} using the SINR from (4) as follows:

[c]In this paper, D2 recovers x_{2n} solely if it has decoded x_{1n} correctly. The criterion for correct decoding is discussed later. Consequently, the remaining interference after removing x_{1n} from the D2 site's received signal does not exist.

$$\Lambda_2^{x_{1n}} = \frac{\psi}{\Xi\left\{\left|\sqrt{1-\psi}x_{2n}+[\tilde{v}_2]_n\right|^2\right\}} = \frac{\psi}{1-\psi+\Phi_{2n}} \quad (6)$$

and x_{2n} with the signal-to-noise ratio (SNR) from the signal, $[\hat{y}_2]_n = [\tilde{y}_2]_n - \sqrt{\psi}x_{1n} = \sqrt{1-\psi}x_{2n} + [\tilde{v}_2]_n$, calculated as

$$\Lambda_2^{x_{2n}} = \frac{1-\psi}{\Xi\left\{\left|[\tilde{v}_2]_n\right|^2\right\}} = \frac{1-\psi}{\Phi_{2n}}. \quad (7)$$

3 | EXACT PERFORMANCE ANALYSIS

In this section, we first analyze the OP, which reflects the probability that the accomplished channel capacity is below the target spectral efficiency, K. Subsequently, the TP analysis is deduced from the OP analysis. Both the proposed TP and OP facilitate prompt performance evaluation without exhaustive simulations.

Note that ZF detection decouples $\mathbf{y}_d$ into N_S symbol streams at Dd, $d = \{1, 2\}$; thus, the OP is identical for any symbol stream. Therefore, we first focus on the n^{th} stream, followed by using its analytical result to obtain the overall OP.

Let Δ_{dn} be the OP of the n^{th} symbol stream in Dd. Then, the overall OP at Dd is

$$\Delta_d = 1-(1-\Delta_{dn})^{N_S}. \quad (8)$$

3.1 | Outage probability of the n^{th} symbol stream at the far user, D1

The OP of the n^{th} symbol stream at Site D1, Δ_{1n}, reflects the probability that Site D1 decodes x_{1n} unsuccessfully. If so, its accomplished channel capacity for recovering x_{1n} subceeds K:

$$\begin{aligned}\Delta_{1n} &= \Pr\{(1-\nu)\log_2(1+\Lambda_1^{x_{1n}}) < K\} \\ &= \Pr\{\Lambda_1^{x_{1n}} < \Lambda_0\} \\ &= \Pr\left\{\frac{\psi}{1-\psi+\Phi_{1n}} < \Lambda_0\right\} \\ &= \begin{cases} F_{\overline{\Phi}_{1n}}(\theta_1), & \frac{\psi}{1-\psi} > \Lambda_0, \\ 1, & \frac{\psi}{1-\psi} \le \Lambda_0, \end{cases}\end{aligned} \quad (9)$$

where $\Lambda_0 = 2^{K/(1-\nu)} - 1$, $\theta_1 = \Lambda_0/[\psi-(1-\psi)\Lambda_0]$, and $\overline{\Phi}_{dn} = 1/\Phi_{dn}$, $d = \{1, 2\}$. Moreover, factor $(1-\nu)$, prior to the logarithm in (9), occurs because the duration of the IT phase is $(1-\nu)L$. Appendix A presents the CDF of $\overline{\Phi}_{dn}$, $F_{\overline{\Phi}_{dn}}(z)$.

Comment 1: Equation (9) implies that because $\Lambda_0 = 2^{K/(1-\nu)} - 1$, D1 incurs a complete outage, $\Delta_{1n} = 1$, when the target spectral efficiency, K, EH duration, ν, and power-splitting factor, ψ, are configured improperly, where $\Lambda_0 \ge \psi/(1-\psi)$. Nevertheless, a complete outage event can be averted by configuring K, ν, and ψ such that $\Lambda_0 < \psi/(1-\psi)$. Thus, nOMMe provides an upper bound to the target spectral efficiency, $K \le -(1-\nu)\log_2(1-\psi)$, to eliminate a complete outage at Site D1.

3.2 | Outage probability of the n^{th} symbol stream at the near user, D2

The OP of the n^{th} symbol stream at Site D2, Δ_{2n}, reflects the probability that Site D2 restores x_{2n} unsuccessfully. Two events can cause D2's outage. First, Site D2 may fail to recover x_{1n} because the attained channel capacity for its recovery subceeds K. Second, Site D2 may recover x_{1n} precisely because the attained channel capacity for its recovery exceeds K, but it fails to decode x_{2n} because the attained channel capacity for its recovery subceeds K:

$$\begin{aligned}\Delta_{2n} &= \Pr\{(1-\nu)\log_2(1+\Lambda_2^{x_{1n}}) < K\} \\ &\quad + \Pr\{(1-\nu)\log_2(1+\Lambda_2^{x_{1n}}) \ge K, \\ &\quad (1-\nu)\log_2(1+\Lambda_2^{x_{2n}}) < K\} \\ &= \Pr\{\Lambda_2^{x_{1n}} < \Lambda_0\} + \Pr\{\Lambda_2^{x_{1n}} \ge \Lambda_0, \Lambda_2^{x_{2n}} < \Lambda_0\} \\ &= 1 - \Pr\{\Lambda_2^{x_{1n}} > \Lambda_0, \Lambda_2^{x_{2n}} > \Lambda_0\}.\end{aligned} \quad (10)$$

Substituting (6) and (7) into (10) yields

$$\begin{aligned}\Delta_{2n} &= 1 - \Pr\left\{\frac{\psi}{1-\psi+\Phi_{2n}} > \Lambda_0 \frac{1-\psi}{\Phi_{2n}} > \Lambda_0\right\} \\ &= \begin{cases} 1 - \Pr\left\{\frac{1}{\Phi_{2n}} > \frac{\Lambda_0}{\psi-(1-\psi)\Lambda_0} \frac{1}{\Phi_{2n}} > \frac{\Lambda_0}{1-\psi}\right\}, & \frac{\psi}{1-\psi} > \Lambda_0 \\ 1, & \frac{\psi}{1-\psi} \le \Lambda_0 \end{cases} \\ &= \begin{cases} F_{\overline{\Phi}_{2n}}(\theta_2), & \frac{\psi}{1-\psi} > \Lambda_0, \\ 1, & \frac{\psi}{1-\psi} \le \Lambda_0, \end{cases}\end{aligned} \quad (11)$$

where $\theta_2 = \max([\Lambda_0/(\psi-(1-\psi)\Lambda_0), \Lambda_0/(1-\psi))$.

Comment 2: Because $\Lambda_0 = 2^{K/(1-\nu)} - 1$, (11) handles the D2's outage, $\Delta_{2n} = 1$, when the target spectral efficiency, K, EH duration, ν, and power-splitting factor, ψ, are configured improperly, where $\Lambda_0 \ge \psi/(1-\psi)$.

Nevertheless, the system configuration can prevent complete outage events by selecting K, ν, and ψ such that $\Lambda_0 < \psi/(1-\psi)$. Thus, nOMMe provides an upper bound to the target spectral efficiency, $K \le -(1-\nu)\log_2(1-\psi)$, to eliminate a complete outage at D2.

Comment 3: Equations (9) and (11) show that the OP of Dd is contingent on multiple specifications: K, ν, ψ, P, N_B, N_S, N_1, N_2, Ω, and τ. Thus, target performance can be attained by appropriately configuring these specifications.

3.3 | Throughput

The throughput of Dd for our nOMMe model with delay-limited communications is expressed as

$$\mathbb{T}_d = N_S(1-\nu)K(1-\Delta_{dn}), \tag{12}$$

where N_S appears in (12) because Site S transmits N_S symbol streams simultaneously.

It can be observed from (12) that the throughput of Dd is also jointly configured by multiple parameters, K, ν, ψ, P, N_B, N_S, N_1, N_2, Ω, and τ, because they affect Δ_{dn}. Consequently, the target throughput is met by flexibly configuring these parameters based on their available value ranges.

4 | PERFORMANCE UPPER BOUNDS

In this section, two performance upper bounds for nOMMe corresponding to two contexts, lEH ($\Omega \to \infty$) and high transmission power ($P \to \infty$), are discussed. These upper bounds reveal the best performance that Dd can attain.

4.1 | Linear energy harvesting ($\Omega \to \infty$)

The OP of the nOMMe for the lEH case is analyzed to quickly compare its counterpart and illustrate its impact on outages and throughput performance. Recall that nlEH reduces to lEH when $\Omega \to \infty$. When $\Omega \to \infty$, (1) is reduced to $P_S \to U\Theta$. Consequently, according to the derivations in Appendix A and the expectation of Θ over $[0,\infty]$, we obtain the OP of Dd as follows:

$$\Delta_{dn}^{\text{lEH}} = \begin{cases} F_{\overline{\Phi}_{dn}}^{\text{lEH}}(\theta_d), & \frac{\psi}{1-\psi} > \Lambda_0, \\ 1, & \frac{\psi}{1-\psi} \le \Lambda_0, \end{cases} \tag{13}$$

where

$$\begin{aligned} F_{\overline{\Phi}_{dn}}^{\text{lEH}}(z) &= \int_0^\infty F_{\overline{\Phi}_{dn}}(z|P_S = U\Theta) f_\Theta(x)dx \\ &= 1 - \frac{\varphi_0^{-N_S N_B}}{\Gamma(N_S N_B)} \sum_{k=0}^{N_d - N_S} \frac{z^k}{k!}\left(\frac{N_S \varepsilon}{\varphi_d U}\right)^k \\ &\quad \times \int_0^\infty x^{N_S N_B - 1 - k} e^{-\frac{x}{\varphi_0} - \frac{N_S \varepsilon z}{\varphi_d U x}} dx \\ &= 1 - \frac{2}{\Gamma(N_S N_B)} \sum_{k=0}^{N_d - N_S} \frac{1}{k!}\left(\frac{N_S \varepsilon z}{\varphi_0 \varphi_d U}\right)^{\frac{N_S N_B + k}{2}} \\ &\quad \times \mathrm{K}_{N_S N_B - k}\left(2\sqrt{\frac{N_S \varepsilon z}{\varphi_0 \varphi_d U}}\right), \end{aligned} \tag{14}$$

where [50, eq. (3.471.9)] is used to compute the last integral in (14).

Therefore, the overall OP of Dd is

$$\Delta_d^{\text{lEH}} = 1 - \left(1 - \Delta_{dn}^{\text{lEH}}\right)^{N_S} \tag{15}$$

and the throughput of Dd is

$$\mathbb{T}_d^{\text{lEH}} = N_S(1-\nu)K\left(1 - \Delta_{dn}^{\text{lEH}}\right). \tag{16}$$

4.2 | High transmit power ($P \to \infty$)

When $P \to \infty$, the energy scavenger becomes saturated, leading to $P_S \to J$. Consequently, by the derivations found in Appendix A, without considering the expectation with respect to P_S, we obtain the OP of the n^{th} symbol stream at Dd as

$$\Delta_{dn}^{\infty} = \begin{cases} F_{\overline{\Phi}_{dn}}^{\infty}(\theta_d), & \frac{\psi}{1-\psi} > \Lambda_0, \\ 1, & \frac{\psi}{1-\psi} \le \Lambda_0, \end{cases} \tag{17}$$

where

$$\begin{aligned} F_{\overline{\Phi}_{dn}}^{\infty}(z) &= F_{\overline{\Phi}_{dn}}(z|P_S = J) \\ &= 1 - e^{-\frac{N_S \varepsilon z}{\varphi_d J}} \sum_{k=0}^{N_d - N_S} \frac{z^k}{k!}\left(\frac{N_S \varepsilon}{\varphi_d J}\right)^k. \end{aligned} \tag{18}$$

Therefore, the overall OP of Dd is

$$\Delta_d^{\infty} = 1 - \left(1 - \Delta_{dn}^{\infty}\right)^{N_S} \tag{19}$$

and the throughput of Dd is

$$\mathbb{T}_d^{\infty} = N_S(1-\nu)K\left(1-\Delta_{dn}^{\infty}\right). \tag{20}$$

5 | DEMONSTRATIVE RESULTS

This section presents numerous theoretical/simulated results to assess the outage and throughput performance of Dd in our proposed nOMMe model using its key parameters. The analytical expressions presented in Sections 3 and 4 were computed to generate the theoretical results (The.). Monte Carlo method [48] was used to produce simulated results (Sim.) for comparison and to corroborate the analytical expressions.[d] Subsequently, nOMMe is compared with its OMMe counterpart, whose analytical results are presented in Appendix B. For demonstration purposes, communication terminals are arbitrarily placed in a two-dimensional plane, and their parameters are listed in Table 3 [49].

5.1 | Transmission-related parameters (P, ν, ψ, K)

Figure 2 reveals the OP of Dd against P for the nOMMe model. The figure shows that the precise (asymptotic) analyses agree with the simulations for the entire range of P (high), confirming the accuracy of the theoretical expressions presented in Sections 3 and 4. Additionally, nlEH agrees with lEH at low P, where the OPs for the nlEH match those of the lEH in the range of $P \le 12.5$ dBW, as expected, owing to nlEH characteristics, where the output powers of nlEH and lEH are similar when their input powers, P, are low. Nevertheless, when P increases, the OPs of lEH are significantly lower than those of nlEH, as anticipated, because the output power of nlEH becomes saturated, whereas that of lEH continues to increase with accreting input power. Thus, the difference in OP between lEH and nlEH considerably increases with an accreting P. Interestingly, P can be optimally selected such that the optimal P is approximately 13.8 dBW, as shown in Figure 2, to minimize the OPs for nlEH. The optimum P represents the lEH-to-nlEH transition.

Figure 3 reveals the throughput of Dd against the target spectral efficiency, K, for the nOMMe model. The figure shows that K can be optimally set to achieve the highest throughput. For example, the highest throughput of Site D1 is achievable by setting the optimum value of $K = 0.4$ bps/Hz for $N_1 = 6$ and $N_2 = 5$. This result makes sense because K balances the OP and the transmission rate. Moreover, Figure 3 demonstrates the throughput improvement provided by increasing N_d as predicted due to the efficacy of the ZF detection as the number of degrees of freedom, $N = N_d - N_S + 1$, increases.

Figure 4 exposes the throughput of Dd against ψ, which represents the power percentage allocated for transmitting information intended for Site D1. Note that $\psi > 0.5$ because x_{1n}. That is, the information intended for Site D1 is allocated more power than x_{2n}, which represents the information intended for Site D2. This figure demonstrates that the throughput of Site D1 increases, whereas that of Site D2 decreases with increasing ψ for

TABLE 3 Frequently used parameters of communication terminals.

Parameter	Value
Position of B	(−10, 0) m
Position of S	(0, 0) m
Position of D1	(50, 0) m
Position of D2	(20, 10) m
Total power of B	$P = 12$ dBW
Noise power	$\varepsilon = -70$ dBm
Path-loss exponent	$\mu = 2.7$
Time-splitting factor	$\nu = 0.4$
Power-splitting factor	$\psi = 0.9$
Power saturation threshold	$\Omega = 0$ dBm
Quantity of antennas at B	$N_B = 3$
Quantity of antennas at S	$N_S = 4$
Fading power at the reference distance	$\rho = 10^{-2}$
Energy conversion efficiency	$\tau = 0.7$

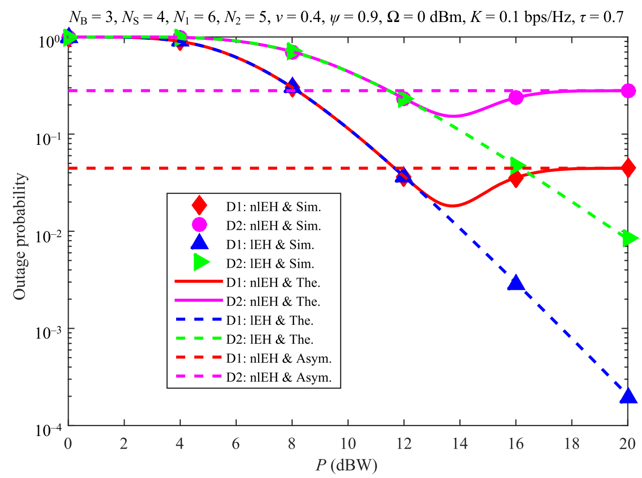

FIGURE 2 Outage probability against the total transmit power of Site B.

[d]Both simulated and theoretical results throughout this paper are generated using MatLab software.

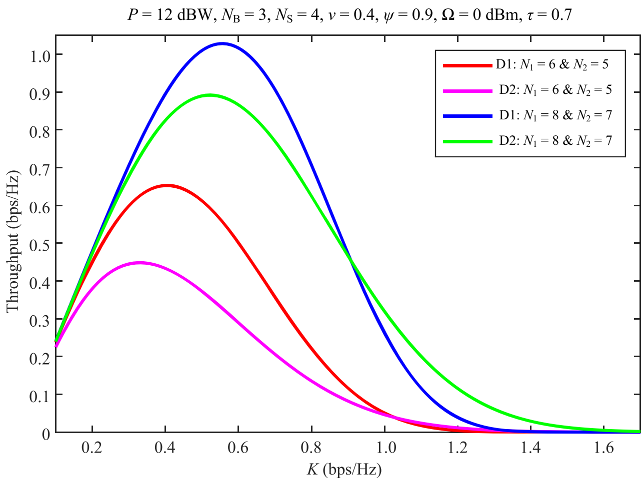

FIGURE 3 Throughput against the target spectral efficiency, K.

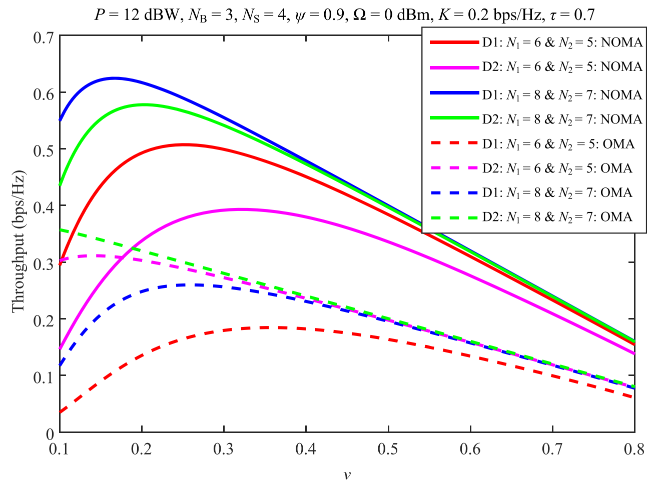

FIGURE 5 Throughput against the time division factor, ν.

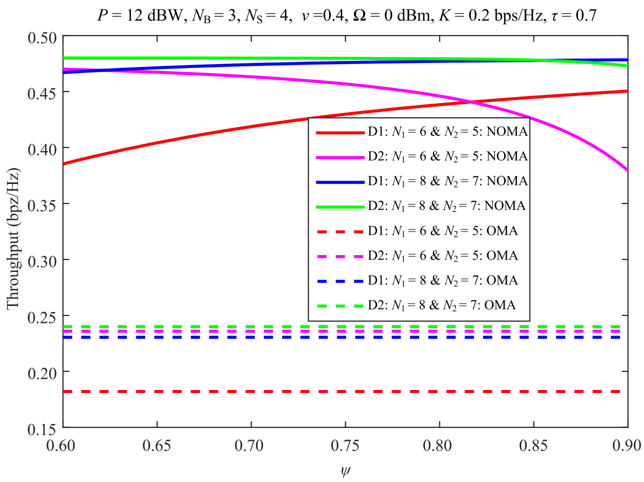

FIGURE 4 Throughput against the power-splitting factor, ψ.

the nOMMe model. This makes sense because increasing ψ accretes the power needed to transmit x_{1n} while decreasing the power needed to transmit x_{2n}. As expected, the OMMe throughput is unchanged with changing ψ. Nevertheless, the nOMMe throughput is significantly higher than that of the OMMe, revealing the improved spectral efficiency of NOMA over its OMA counterpart. Furthermore, accreting the number of antennas at Dd improves the throughput for both nOMMe and OMMe. That is, the throughput in the cases of $N_1 = 8$ and $N_2 = 7$ is higher than that in the cases of $N_1 = 6$ and $N_2 = 5$. This result is reasonable because increasing N_d makes the ZF detection at Dd more efficient.

Figure 5 reveals the throughput of Dd against ν, which reflects the time percentage for EH. It can be seen that ν can be optimized to achieve the highest throughput for both nOMMe and OMMe. The optimal value of ν balances the time needed for the EH and IT phases. As in Figure 4, Figure 5 reveals the superiority of the nOMMe over the OMMe and the respective throughput improvements from increasing N_d for both.

5.2 | Energy harvesting-related parameters (N_B, τ, N_S, Ω)

Figure 6 presents the OP of Dd versus the power saturation threshold, Ω, for the nOMMe. As expected, the performance of Dd is considerably ameliorated by accreting Ω. Additionally, it is saturated at a high Ω, where the nlEH approaches the lEH, as anticipated. Thus, the analysis in Section 4.1 is validated. Moreover, the lEH outperforms the nlEH. Furthermore, Figure 6 demonstrates the performance improvement with increasing N_d, as predicted due to the efficacy of the ZF detection.

Figure 7 shows the throughput of Dd against the number of antennas, N_S, at Site S. It was expected that increasing N_S would help Site S harvest more energy and improve the throughput of Dd for both nOMMe and OMMe models. Figure 7 supports this improvement, where the throughput increases considerably with an increasing N_S for both nOMMe and OMMe models. However, a high value of N_S reduces the effectiveness of ZF detection owing to the decrease in the number of degrees of freedom; thus, the throughput decreases after its peak value as N_S continues to increase. For instance, Figure 7 shows that the throughputs of Sites D2 and D1 reach their peak values at $N_S = 7$ and $N_S = 6$ for nOMMe and OMMe, respectively. Moreover, the nOMMe model attains a significantly higher throughput than does the OMMe model, again verifying the efficacy of NOMA compared with its OMA counterpart.

Figure 8 exposes the throughput of Dd against the energy conversion efficiency, τ, at Site S. It was anticipated that increasing τ would assist Site S in scavenging

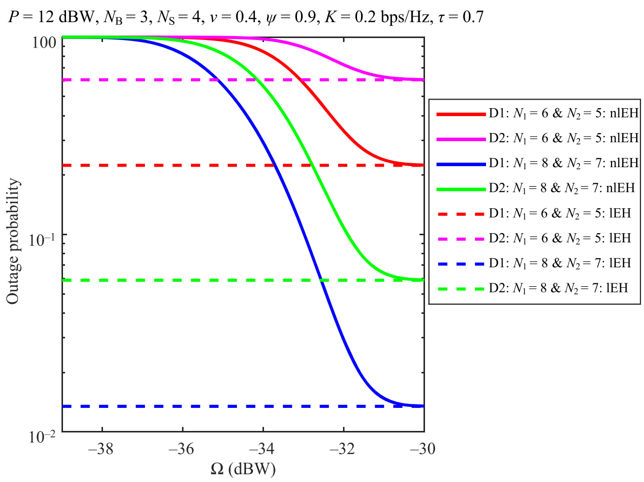

FIGURE 6 Outage probability against the power saturation threshold, Ω.

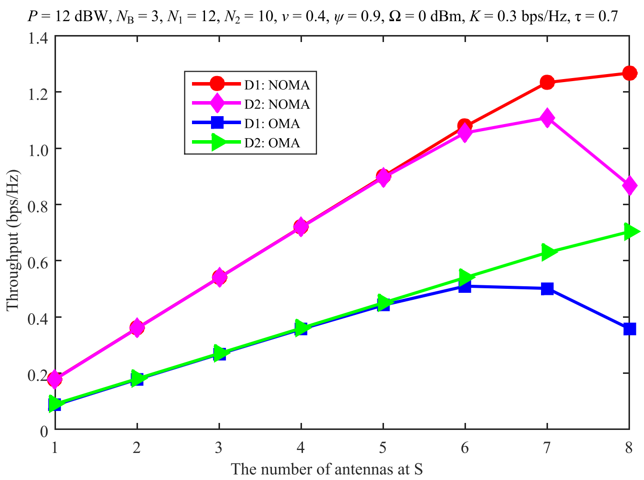

FIGURE 7 Throughput versus N_S.

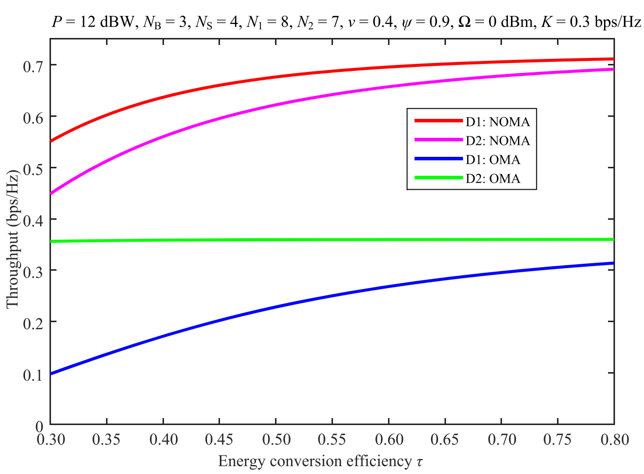

FIGURE 8 Throughput against τ.

more energy, thereby improving the throughput of D*d* for both nOMMe and OMMe models. Figure 8 demonstrates this improvement, where the throughput increases with an increasing τ for both models. Furthermore, the

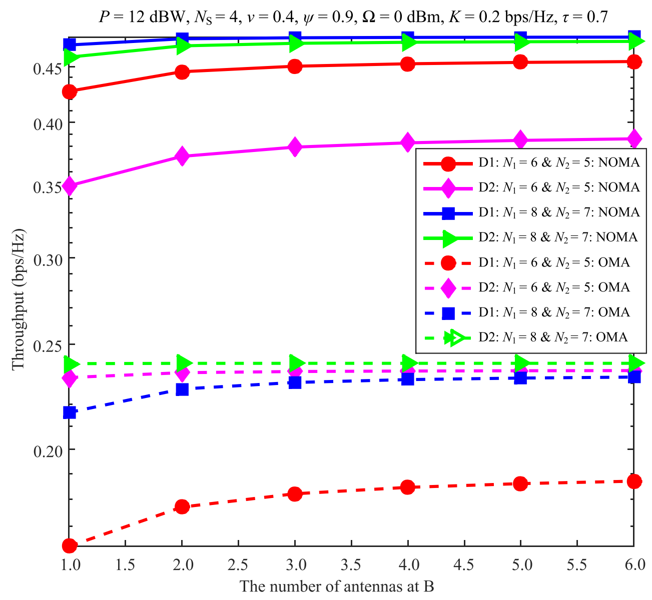

FIGURE 9 Throughput against the quantity of antennas at Site B.

nOMMe model attains a significantly higher throughput than does the OMMe model, again verifying the efficacy of NOMA compared with its OMA counterpart.

Figure 9 demonstrates the throughput of D*d* against N_B. It was anticipated that accreting N_B would aid Site S in harvesting energy more efficiently, thus improving the throughput of both nOMMe and OMMe models. Figure 9 reflects this improvement, where the throughput increases with an increasing N_B for both nOMMe and OMMe models. Like the results shown in Figure 4, Figure 9 illustrates the superiority of the nOMMe model to the OMMe model and the throughput improvements when increasing N_d for both.

6 | CONCLUSIONS

In this study, two key performance metrics, TP and OP, were analyzed for the proposed nOMMe model, which considers the practical concerns of the nlEH and the multiantenna users. The proposed analysis was represented in a closed form, which directly provides insights into the proposed nOMMe model, leading to its full performance evaluation under different crucial parameters. Multiple results reveal that nlEH considerably mitigates system performance, and the desired performance is achieved by configuring multiple parameters, K, ψ, ν, P, N_B, N_S, N_1, N_2, Ω, and τ. Remarkably, nOMMe can avert complete outages by fine-tuning K, ν, and ψ, which ensures optimum performance with optimal N_S and P. Moreover, their increase considerably improves overall system performance. Furthermore, the proposed nOMMe model is superior to its traditional OMMe counterpart.

Although this study analyzes the TP and OP metrics of the nOMMe model for the first time, it still has some limitations. Specifically, this study investigates typical Rayleigh fading channels and illustrates MIMO detection using only ZF detection. As such, more general fading channels, such as Nakagami-*m* fading [9], may reflect a better match to the field measurement data and better-but-more complicated MIMO detectors, such as the minimum mean squared error detector. These aspects should be considered in future works. However, for more general fading channels and complicated MIMO detectors, the SINR statistics are complex to derive. A feasible technique to address this is to approximate or bind the SINRs to a simpler form, from which closed-form statistics can be derived. Furthermore, this study investigates only the nlEH model of [13]. Therefore, our future work will consider other practical and complicated nlEH models [14–19]. Nevertheless, other practical and complicated nlEH models cause the P_S statistic to differ from (1). Thus, it is difficult to derive, which causes the performance analysis to become intractable. To overcome this issue, approximating or simplifying P_S may be sufficient.

ACKNOWLEDGMENTS

This research was funded by the Vietnam National University Ho Chi Minh City (VNU-HCM) under grant number B2023-20-08.

CONFLICT OF INTEREST STATEMENT

The authors declare that there are no conflicts of interest.

ORCID

Khuong Ho-Van https://orcid.org/0000-0001-7044-4131

REFERENCES

1. A. Y. Alhilal, B. Finley, T. Braud, D. Su, and P. Hui, *Street smart in 5G: Vehicular applications, communication, and computing*, IEEE Access **10** (2022), 105631–105656.
2. B. Ozpoyraz, A. T. Dogukan, Y. Gevez, U. Altun, and E. Basar, *Deep learning-aided 6G wireless networks: A comprehensive survey of revolutionary PHY architectures*, IEEE Open J. Commun. Soc. **3** (2022), 1749–1809.
3. X. Bai and X. Gu, *NOMA assisted semi-grant-free scheme for scheduling multiple grant-free users*, IEEE Syst. J. 17 (2023), no. 2, 3294–3305.
4. J. Li, H. H. Chen, and Q Guo, *On the performance of NOMA systems with different user grouping strategies*, IEEE Wire. Commun. To appear.
5. M. M. Fakharian, *RF Energy harvesting using high impedance asymmetric antenna array without impedance matching network*, Radio Sci. **56** (2021), no. 3, 1–10.
6. N. A. Eltresy, M. Abd Elhamid, D. M. Elsheakh, H. M. Elhennawy, and E. A. Abdallah, *Silver sandwiched ITO based transparent antenna array for RF energy harvesting in 5G mid-range of frequencies*, IEEE Access **9** (2021), 49476–49486.
7. D. Wang, F. Zhou, and V. C. Leung, *Primary privacy preserving with joint wireless power and information transfer for cognitive radio networks*, IEEE Trans. Cog. Commun. Netw. **6** (2020), no. 2, 683–693.
8. L. Ge, G. Chen, Y. Zhang, J. Tang, J. Wang, and J. A. Chambers, *Performance analysis for multihop cognitive radio networks with energy harvesting by using stochastic geometry*, IEEE IoT J. **7** (2020), no. 2, 1154–1163.
9. N. Pham-Thi-Dan, K. Ho-Van, T. Do-Dac, S. Vo-Que, and S. Pham-Ngoc, *Security analysis for cognitive radio network with energy scavenging capable relay over Nakagami-m fading channels*, (International Symposium on Electrical and Electronics Engineering, Ho Chi, Minh, Vietnam), 2019, pp. 68–72.
10. M. Bouabdellah, F. El Bouanani, P. C. Sofotasios, S. Muhaidat, D. B. Da Costa, K. Mezher, H. Ben-Azza, and G. K. Karagiannidis, *Cooperative energy harvesting cognitive radio networks with spectrum sharing and security constraints*, IEEE Access **7** (2019), 173329–173343.
11. F. Khennoufa, A. Khelil, K. Rabie, H. Kaya, and X. Li, *An efficient hybrid energy harvesting protocol for cooperative NOMA systems: Error and outage performance*, Phys. Commun. **58** (2023), 1–12.
12. N. K. Largani and B. Akhbari, *Enhancing secrecy performance of energy harvesting NOMA systems using IoT user scheduling under untrusted users*, IET Commun. **16** (2022), 2208–2218.
13. S. Solanki, P. K. Upadhyay, D. B. Da Costa, H. Ding, and J. M. Moualeu, *Performance analysis of piece-wise linear model of energy harvesting-based multiuser overlay spectrum sharing networks*, IEEE Open J. Commun. Soc. **1** (2020), 1820–1836.
14. D. Wang, F. Rezaei, and C. Tellambura, *Performance analysis and resource allocations for a WPCN with a new nonlinear energy harvester model*, IEEE Open J. Commun. Soc. **1** (2020), 1403–1424.
15. L. Ni, X. Da, H. Hu, Y. Yuan, Z. Zhu, and Y. Pan, *Outage-constrained secrecy energy efficiency optimization for CRNs with non-Linear energy harvesting*, IEEE Access **7** (2019), 175213–175221.
16. M. Babaei, Ü. Aygölü, M. Baaran, and L. Durak-Ata, *BER performance of full-duplex cognitive radio network with nonlinear energy harvesting*, IEEE Trans. Green Commun. Netw. **4** (2020), no. 2, 448–460.
17. D. Wang and S. Men, *Secure energy efficiency for NOMA based cognitive radio networks with nonlinear energy harvesting*, IEEE Access **6** (2018), 62707–62716.
18. F. Wang and X. Zhang, *Secure resource allocation for polarization-based non-linear energy harvesting over 5G cooperative CRNs*, IEEE Wire. Commun. Lett. To appear.
19. Z. Zhu, N. Wang, W. Hao, Z. Wang, and I. Lee, *Robust beamforming designs in secure MIMO SWIPT IoT networks with a nonlinear channel model*, IEEE IoT J. **8** (2021), no. 3, 1702–1715.
20. Y. Jiang, M. K. Varanasi, and J. Li, *Performance analysis of ZF and MMSE equalizers for MIMO systems: An in-depth study of the high SNR regime*, IEEE Trans. Info. The. **57** (2011), no. 4, 2008–2026.
21. A. Khazali, D. Tarchi, M. G. Shayesteh, H. Kalbkhani, and A. Bozorgchenani, *Energy efficient uplink transmission in cooperative mmWave NOMA networks with wireless power transfer*, IEEE Trans. Veh. Tech. **71** (2022), no. 1, 391–405.

22. C. K. Singh, V. Singh, P. K. Upadhyay, and M. Lin, *Energy harvesting in overlay cognitive NOMA systems with hardware impairments*, IEEE Sys. J. **16** (2022), no. 2, 2648–2659.
23. A. K. Shukla, V. Singh, P. K. Upadhyay, A. Kumar, and J. M. Moualeu, *Performance analysis of energy harvesting-assisted overlay cognitive NOMA systems with incremental relaying*, IEEE OJCOMS **2** (2021), 1558–1576.
24. Y. Liu, Y. Ye, H. Ding, F. Gao, and H. Yang, *Outage performance analysis for SWIPT-based incremental cooperative NOMA networks with non-linear harvester*, IEEE Commun. Lett. **24** (2020), no. 2, 287–291.
25. Q. N. Le, A. Yadav, N. P. Nguyen, O. A. Dobre, and R. Zhao, *Full-duplex non-orthogonal multiple access cooperative overlay spectrum-sharing networks with SWIPT*, IEEE Trans. Green Commun. Netw. **5** (2021), no. 1, 322–334.
26. X. Liu, Y. Guo, and T. S. Durrani, *Simultaneous wireless information and power transfer based on symbol allocation for GFDM-NOMA cooperative communications*, IEEE Wire. Commun. Lett. **11** (2022), no. 2, 333–337.
27. D. T. Do, A. T. Le, Y. Liu, and A. Jamalipour, *User grouping and energy harvesting in UAV-NOMA system with AF/DF relaying*, IEEE Trans. Veh. Tech. **70** (2021), no. 11, 11855–11868.
28. K. Agrawal, M. F. Flanagan, and S. Prakriya, *NOMA with battery-assisted energy harvesting full-duplex relay*, IEEE Trans. Veh. Tech. **69** (2020), no. 11, 13952–13957.
29. L. Ma, E. Li, and Q Yang, *On the performance of full-duplex cooperative NOMA with non-linear EH*, IEEE Access **9** (2021), 145968–145976.
30. V. Aswathi and A. V. Babu, *Outage and throughput analysis of full-duplex cooperative NOMA system with energy harvesting*, IEEE Trans. Veh. Tech. **70** (2021), no. 11, 11648–11664.
31. Q. Si, M. Jin, T. A. Tsiftsis, N. Zhao, and X. Wang, *Cooperative SM-based NOMA scheme with SWIPT*, IEEE Trans. Veh. Tech. **70** (2021), no. 6, 6195–6199.
32. C. E. García, M. R. Camana, and I Koo, *Low-complexity PSO-based resource allocation scheme for cooperative non-linear SWIPT-enabled NOMA*, IEEE Access **10** (2022), 34207–34220.
33. T. N. Tran, T. P. Vo, P. Fazio, and M. Voznak, *SWIPT model adopting a PS framework to aid IoT networks inspired by the emerging cooperative NOMA technique*, IEEE Access **9** (2021), 61489–61512.
34. X. Li, Q. Wang, M. Liu, J. Li, H. Peng, M. J. Piran, and L. Li, *Cooperative wireless-powered NOMA relaying for B5G IoT networks with hardware impairments and channel estimation errors*, IEEE IoT J. **8** (2021), no. 7, 5453–5467.
35. S. Bisen, P. Shaik, and V Bhatia, *On performance of energy harvested cooperative NOMA under imperfect CSI and imperfect SIC*, IEEE Trans. Veh. Tech. **70** (2021), no. 9, 8993–9005.
36. C. Zhai, Y. Li, X. Wang, and Z. Yu, *Nonorthogonal multiple access with energy harvesting-based alternate relaying*, IEEE Syst. J. **16** (2022), no. 1, 327–338.
37. R. Lei, D. Xu, and I. Ahmad, *Secrecy outage performance analysis of cooperative NOMA networks with SWIPT*, IEEE Wire. Commun. Lett. **10** (2021), no. 7, 1474–1478.
38. X. Li, J. Li, and L. Li, *Performance analysis of impaired SWIPT NOMA relaying networks over imperfect Weibull channels*, IEEE Syst. J. **14** (2020), no. 1, 669–672.
39. M. Aldababsa and E. Basar, *Joint transmit-and-receive antenna selection system for MIMO-NOMA with energy harvesting*, IEEE Syst. J. **16** (2022), no. 3, 4139–4148.
40. B. Lyu, P. Ramezani, D. T. Hoang, and A. Jamalipour, *IRS-assisted downlink and uplink NOMA in wireless powered communication networks*, IEEE Trans. Veh. Tech. **71** (2022), no. 1, 1083–1088.
41. Q. Wu, X. Zhou, and R. Schober, *IRS-assisted wireless powered NOMA: Do we really need different phase shifts in DL and UL*, IEEE Wire. Commun. Lett. **10** (2021), no. 7, 1493–1497.
42. D. Zhang, Q. Wu, M. Cui, G. Zhang, and D. Niyato, *Throughput maximization for IRS-assisted wireless powered hybrid NOMA and TDMA*, IEEE Wire. Commun. Lett. **10** (2021), no. 9, 1944–1948.
43. F. D. Ardakani, R. Huang, and V. W. Wong, *Joint device pairing, reflection coefficients, and power control for NOMA backscatter systems*, IEEE Trans. Veh Tech. **71** (2022), no. 4, 4396–4411.
44. F. Zhao, W. Xu, and W. Xiang, *Integrated satellite-terrestrial networks with coordinated C-NOMA and relay transmission*, IEEE Sys. J. **16** (2022), no. 4, 5270–5280.
45. Study on Downlink multiuser superposition transmission for LTE, 3GPP, 2015. Shanghai, China.
46. G. Chen, L. Qiu, and C. Ren, *On the performance of cluster-based MIMO NOMA in multi-cell dense networks*, IEEE Trans. Commun. **68** (2020), no. 8, 4773–4787.
47. Z. Ding, P. Fan, and H. V. Poor, *Impact of user pairing on 5G nonorthogonal multiple-access downlink transmissions*, IEEE Trans. Veh. Tech. **65** (2016), 6010–6023.
48. N. T. Thomopoulos, *Essentials of Monte Carlo simulation: Statistical methods for building simulation models*, Springer, New York Heidelberg Dordrecht London, 2013.
49. A. Hakimi, M. Mohammadi, Z. Mobini, and Z. Ding, *Full-duplex non-orthogonal multiple access cooperative spectrum-sharing networks with non-linear energy harvesting*, IEEE Trans. Veh. Tech. **69** (2020), no. 10, 10925–10936.
50. I. S. Gradshteyn and I. M. Ryzhik, *Table of integrals, series and products*, 6th ed., Academic, San Diego, CA, 2000.
51. M. Abramowitz and I. A. Stegun, *Handbook of mathematical functions with formulas, graphs, and mathematical tables, Tenth printing ed*, U.S. Government Printing Office, Washington, DC, USA, 1972.

AUTHOR BIOGRAPHIES

Toi Le-Thanh was born in Tay Ninh City, Vietnam. He received his MS degree from the Ho Chi Minh City University of Technology, Vietnam, in 2006. He has been a lecturer at the Ho Chi Minh City University of Food Industry (HUFI) since 2003. His research interests include wireless communications, null conventional logic, asynchronous circuit design, and low-power circuit design.

Khuong Ho-Van received his BE (first-rank honor) and MS degrees in electronics and telecommunications engineering from the Ho Chi Minh City University of Technology, Vietnam, in 2001 and 2003, respectively. He received his PhD degree in electrical engineering from the University of Ulsan, Korea, in 2007. From 2007 to 2011, he worked at McGill University, Canada, as a postdoctoral fellow. He is currently an associate professor at the Ho Chi Minh City University of Technology. His major research interests include modulation and coding techniques, diversity techniques, digital signal processing, energy harvesting, physical-layer security, and cognitive radio.

How to cite this article: T. Le-Thanh and K. Ho-Van, *Nonorthogonal multiple access multiple input multiple output communications with harvested energy: Performance evaluation*, ETRI Journal **46** (2024), 432–445. DOI 10.4218/etrij.2023-0048

APPENDIX A: THE CDF OF $\overline{\Phi}_{dn}$

As per [20], $\overline{\Phi}_{dn} = \frac{1}{\Phi_{dn}}$ is rewritten as $\overline{\Phi}_{dn} = \frac{P_S/(N_S\varepsilon)}{\left[\left(\mathbf{H}_d^*\mathbf{H}_d\right)^{-1}\right]_{nn}}$ whose PDF conditioned on P_S is expressed as

$$f_{\overline{\Phi}_{dn}}(z|P_S) = \frac{z^{N_d-N_S}e^{-z/\Psi_d}}{(N_d-N_S)!\Psi_d^{N_d-N_S+1}}, \tag{A1}$$

where $\Psi_d = \varphi_d P_S / N_S\varepsilon$.

Therefore, the CDF of $\overline{\Phi}_{dn}$ conditioned on P_S is given by

$$\begin{aligned} F_{\overline{\Phi}_{dn}}(z|P_S) &= \int_0^z f_{\overline{\Phi}_{dn}}(x|P_S)dx \\ &= \frac{\Psi_d^{N_S-N_d-1}}{(N_d-N_S)!}\int_0^z x^{N_d-N_S}e^{-x/\Psi_d}dx \\ &= 1 - e^{-z/\Psi_d}\sum_{k=0}^{N_d-N_S}\frac{z^k}{k!\Psi_d^k}, \end{aligned} \tag{A2}$$

where the second integral is solved using [50, eq. (3.351.1)].

The CDF of $\overline{\Phi}_{dn}$ is defined as

$$\begin{aligned} F_{\overline{\Phi}_{dn}}(z) &= \Pr\{\overline{\Phi}_{dn} < z\} \\ &= \mathrm{E}_{P_S}\{\Pr\{\overline{\Phi}_{dn} < z|P_S\}\} \\ &= \mathrm{E}_{P_S}\left\{F_{\overline{\Phi}_{dn}}(z|P_S)\right\}. \end{aligned} \tag{A3}$$

Using P_S in (1), we simplify (A3) as follows:

$$\begin{aligned} F_{\overline{\Phi}_{dn}}(z) &= \underbrace{\int_0^G F_{\overline{\Phi}_{dn}}(z|P_S = U\Theta)f_\Theta(x)dx}_{\mathcal{A}} \\ &\quad + \underbrace{\int_G^\infty F_{\overline{\Phi}_{dn}}(z|P_S = J)f_\Theta(x)dx}_{\mathcal{B}} \end{aligned}. \tag{A4}$$

To compute (A4), we must find the CCDF, CDF, and PDF of Θ. Because $\Theta = \|\mathbf{H}_0\|^2 = \sum_{u=1}^{N_S}\sum_{v=1}^{N_B}\left|[\mathbf{H}_0]_{uv}\right|^2$ is the sum of $N_B N_S$ with iid exponential rv's with mean φ_0, Θ is gamma-distributed [25] with the PDF as $f_\Theta(x) = \frac{\varphi_0^{-N_B N_S}}{\Gamma(N_B N_S)}x^{N_B N_S - 1}e^{-\frac{x}{\varphi_0}}$, the CDF as $F_\Theta(x) = \frac{\gamma(N_B N_S, x/\varphi_0)}{\Gamma(N_B N_S)}$, and the CCDF as $\overline{F}_\Theta(x) = 1 - \frac{\gamma(N_B N_S,\, x/\varphi_0)}{\Gamma(N_B N_S)}$. Invoking (A2) and $f_\Theta(x)$, we obtain a closed-form representation of the first term in (A4) as follows:

$$\begin{aligned} \mathcal{A} &= \int_0^G\left(1 - e^{-z/\left(\frac{\varphi_d Ux}{N_S\varepsilon}\right)}\sum_{k=0}^{N_d-N_S}\frac{z^k}{k!}\left(\frac{\varphi_d Ux}{N_S\varepsilon}\right)^{-k}\right)f_\Theta(x)dx \\ &= F_\Theta(G) - \frac{\varphi_0^{-N_S N_B}}{\Gamma(N_S N_B)}\sum_{k=0}^{N_d-N_S}\frac{z^k}{k!}\left(\frac{N_S\varepsilon}{\varphi_d U}\right)^k \\ &\quad \times \int_0^G e^{-\frac{x}{\varphi_0}-\frac{N_S\varepsilon z}{\varphi_d Ux}}x^{N_S N_B - 1 - k}dx \\ &\simeq \frac{\gamma(N_B N_S, G/\varphi_0)}{\Gamma(N_B N_S)} - \frac{\varphi_0^{-N_S N_B}}{\Gamma(N_S N_B)}\sum_{k=0}^{N_d-N_S}\frac{z^k}{k!}\left(\frac{N_S\varepsilon}{\varphi_d U}\right)^k \\ &\quad \times \frac{G}{2}\sum_{u=1}^{Q}\frac{\pi}{Q}\sqrt{1-\vartheta_u^2}\,e^{-\frac{\zeta_u}{\varphi_0}-\frac{N_S\varepsilon z}{\varphi_d U\zeta_u}}\zeta_u^{N_S N_B - 1 - k}, \end{aligned} \tag{A5}$$

where $\vartheta_u = \cos\left(\frac{2u-1}{2Q}\pi\right)$ and $\zeta_u = \frac{G}{2}(\vartheta_u + 1)$. The Gaussian–Chebyshev quadrature in [51] with Q representing the complexity–accuracy trade-off is invoked to approximate the last integral in (A5). $Q = 150$, which warrants exceptionally high accuracy, is used to compute the theoretical results in Section 5.

Similarly, by invoking (A2) and $f_{\Theta}(x)$, we obtain the closed-form representation of the second term in (A4) as follows:

$$\begin{aligned}\mathcal{B} &= F_{\overline{\Phi}_{dn}}(z|P_{\mathrm{S}}=J)\overline{F}_{\Theta}(G)\\ &= \left[1-e^{-\frac{N_{\mathrm{S}}\varepsilon z}{\varphi_d J}}\sum_{k=0}^{N_d-N_{\mathrm{S}}}\frac{z^k}{k!}\left(\frac{N_{\mathrm{S}}\varepsilon}{\varphi_d J}\right)^k\right]\\ &\times\left(1-\frac{\gamma(N_{\mathrm{B}}N_{\mathrm{S}},G/\varphi_0)}{\Gamma(N_{\mathrm{B}}N_{\mathrm{S}})}\right).\end{aligned} \tag{A6}$$

Substituting (A5) and (A6) into (A4), we obtain the closed form, $F_{\overline{\Phi}_{dn}}(z)$, thus completing the presentation in Appendix A.

APPENDIX B: ORTHOGONAL MULTIPLE ACCESS MIMO COMMUNICATIONS WITH HARVESTED ENERGY

In the OMMe, the IT phase is separated equally into two stages, each with a duration of $\frac{1-\nu}{2}L$, during which S transmits information sequentially and directly to D1 and D2. As a result, Dd receives the signal as $\mathbf{y}_d=\mathbf{H}_d\sqrt{\frac{P_{\mathrm{S}}}{N_{\mathrm{S}}}}\mathbf{s}_d+\mathbf{v}_d$, where $\mathbf{s}_d=[x_{d1}\ \ldots\ x_{dN_{\mathrm{S}}}]^{\mathrm{T}}$ is the $N_{\mathrm{S}}\times 1$ signal vector of N_{S} symbols intended for Dd, $(\cdot)^{\mathrm{T}}$ is the transpose operator, and $d=\{1,2\}$. Then, Dd performs only the ZF detection; hence, the SNR for Dd to detect x_{dn} is $\Lambda_d^{x_{dn}}=\overline{\Phi}_{dn}$. Accordingly, the channel capacity achieved by Dd is $\mathsf{R}_d=\frac{1-\nu}{2}\log_2(1+\overline{\Phi}_{dn})$, where factor $\frac{1-\nu}{2}$ is performed before the logarithm, as S transmits information to Dd only in $\frac{1-\nu}{2}L$. Consequently, the OP of the n^{th} symbol stream at Dd is

$$\Delta_{dn}^{\mathrm{OMA}}=\Pr\{\mathrm{R}_d<K\}=\Pr\{\overline{\Phi}_{dn}<\tilde{\Lambda}_0\}=F_{\overline{\Phi}_{dn}}(\tilde{\Lambda}_0), \tag{B1}$$

where $\tilde{\Lambda}_0=2^{2K/(1-\nu)}-1$.

Therefore, the overall OP of Dd is

$$\Delta_d^{\mathrm{OMA}}=1-\left(1-\Delta_{dn}^{\mathrm{OMA}}\right)^{N_{\mathrm{S}}}, \tag{B2}$$

and the throughput of Dd is

$$\mathbb{T}_d^{\mathrm{OMA}}=N_{\mathrm{S}}\frac{1-\nu}{2}K\left(1-\Delta_{dn}^{\mathrm{OMA}}\right). \tag{B3}$$

OMMe is considered a baseline communication scheme. Given the closed-form expressions of Δ_d^{OMA} and $\mathbb{T}_d^{\mathrm{OMA}}$, it is convenient to compare the performances of OMMe and nOMMe models, from which the advantages of each can be promptly revealed.